Supplementary Information

Fluorination fine-tunes the electronic structure and hydrophobic microenvironment of metal-free nitrogen-doped carbon for efficient electrocatalytic CO_2 reduction

Weiqi Liu, Chuangchuang Yang, Peiyao Bai, Shilin Wei, Haoquan Wang, Shiyong Xu and Lang Xu*

MOE Key Laboratory of Coal Processing and Efficient Utilization, School of Chemical Engineering and Technology, China University of Mining and Technology, 1 Daxue Road, Xuzhou, Jiangsu, 221116, China

*Corresponding author. *E-mail address: lang.xu@cumt.edu.cn* (L. Xu)

Experimental

Chemicals

Wheat straw was collected on the University campus and pulverized into a fine powder before use. Potassium hydroxide (KOH), potassium bicarbonate ($KHCO_3$), N,N-dimethylformamide, and perfluoropropylvinyl ether (PPVE) were purchased from Shanghai Titan Scientific Co. Ltd. Nafion solution (5 wt%) and sodium fluoride (NaF) was purchased from Sigma-Aldrich Chemical Reagent Co. Ltd. Fumion solution (FAA-3-SOLUT-10) were purchased from Suzhou Sinero Technology Co. Ltd. 2-Methylimidazole was purchased from Shanghai Aladdin Bio-Chem Technology Co. Ltd. Hydrochloric acid (HCl) was purchased from Xilong Science Co. Ltd. Ultrapure water (18.2 MΩ cm) was used throughout. All chemicals were used as received without further purification.

Preparations

Wheat straw powder (3 g) and KOH (3 g) were added to 100 mL of ultrapure water and stirred at 80 °C for 2 h. The mixture was then dried overnight at 80 ºC in an oven. The dried mixture was placed in a tube furnace, heated to 900 °C at a rate of 5 °C min^{-1} under N_2 atmosphere, and held at this temperature for 2 h. After cooling to room temperature, the resulting black solid was immersed in 1 M HCl solution, stirred vigorously at 50 °C for 1 h, filtered, and washed repeatedly with ultrapure water. The obtained porous carbon was dried overnight at 80 ºC and denoted as PC.

For the preparation of porous carbon doped with N and F (PCNF), PC (0.1 g) and 2-methylimidazole (0.82 g) were added in 30 mL of ultrapure water. The mixture was heated to 50 °C and vigorously stirring for 0.5 h, followed by the addition of 3 mL of Nafion solution (5 wt%) and further stirred for 1 h. The resulting solution was dried at 80 ºC for 24 h, and the solid mixture was pyrolyzed at 700 ºC for 2 h under N_2 atmosphere (heating rate: 5 °C min^{-1}). The product was then

washed with 1 M HCl at 50 ℃ for 1 h, filtered, and dried at 80 °C overnight. The obtained catalyst was denoted as PCNF.

The reference samples, porous carbon doped with N (PCN) and porous carbon doped with F (PCF), were prepared following the same procedure, except that Nafion solution was not used for PCN and that 2–methylimidazole was not used for PCF. To evaluate the advantages of Nafion as the F source, we prepared two additional porous carbon samples doped with N and F following the same procedure as PCNF, except that 3 mL of Nafion solution was replaced with 0.12 g of PPVE and 0.18 g of NaF, respectively. The mass of F element in 0.12 g of PPVE and 0.18 g of NaF equals that in 3 mL of Nafion solution (5 wt%). These samples are designated PCNF-PPVE and PCNF-NaF. Additionally, to exclude any contribution from residual fluorinated surface species to the ECR activity and hydrophobicity of PCNF, a portion of PCNF was treated with Ar plasma for 10 minutes to remove its outermost surface layers. The resulting material is designated PCNF-plasma.

Characterization

Transmission electron microscopy (TEM) images were acquired using an FEI Talos 200S. N_2 adsorption-desorption isotherms were collected at 77 K using a Quantachrome Autosorb-iQ physical sorption analyzer. Surface chemical compositions were analyzed by X-ray photoelectron spectroscopy (XPS, Thermo Scientific K-Alpha) with Al Kα radiation (1486.6 eV). X-ray diffraction (XRD) patterns were recorded on a Bruker D2 Phaser diffractometer with Cu Kα radiation (λ = 1.5406 Å). Raman spectra were obtained using a Bruker Senterra confocal Raman spectrometer with a 532 nm laser. Water contact angles were measured on a DSA-X optical contact angle apparatus. Reaction intermediates were probed by *in situ* attenuated total reflectance-surface enhanced infrared absorption spectroscopy (ATR-SEIRAS, Thermo Scientific Nicolet iS20).

Electrochemical measurements in an H-type cell

Working electrodes were prepared by dispersing 3 mg of catalyst, 20 μL of Nafion solution, and 480 μL of N,N-dimethylformamide under sonication for 0.5 h. The resulting homogeneous dispersion (40 μL) was drop-coated onto carbon paper (TGP-H-060, 0.5 cm^2), yielding a catalyst loading of approximately 0.48 mg cm^{-2}. To exclude any influence of the Nafion binder on the electrochemical performance, we also prepared working electrodes using PCNF and PCNF-plasma as catalysts and an F-free Fumion solution (FAA-3-SOLUT-10) as the binder, following the same procedure. These electrodes are designated PCNF-Fumion and PCNF-plasma-Fumion, respectively.

Electrochemical measurements were first conducted in a typical H-type cell with a three-electrode configuration using an electrochemical workstation (IviumStat.h, Ivium Technologies). The cathode and anode chambers were separated by a proton exchange membrane (Nafion 115). A platinum sheet acts as the counter electrode and a Ag/AgCl electrode (3.5 M KCl) was used as the reference electrode. The electrolyte was 0.5 M $KHCO_3$ solution. Before each test, CO_2 was bubbled through the catholyte for 0.5 h to remove other gases; continuous CO_2 flow (10 mL min^{-1}) was maintained during electrolysis. All potentials were converted to the reversible hydrogen electrode (RHE) using the following equation:

$$E\ (\text{vs. RHE}) = E\ (\text{vs. Ag/AgCl}) + 0.1989\ \text{V} + 0.0592 \times \text{pH} \quad (1)$$

Linear sweep voltammetry (LSV) was performed in N_2- or CO_2-saturated 0.5 M $KHCO_3$ at a scan rate of 5 mV s^{-1}. Chronoamperometry was conducted at potentials ranging from –0.5 to –1.1 V to evaluate ECR selectivity and activity. Gaseous products were analyzed by an on-line gas chromatography (GC, Agilent 7890B) equipped with a thermal conductivity detector (TCD), a flame ionization detector (FID), and a methanizer which can convert CO to CH_4 for enhanced FID sensitivity. Liquid products were analyzed by ^1H nuclear magnetic resonance (NMR) spectroscopy

(Bruker 600 MHz). An aliquot of 500 μL of the post-electrolysis electrolyte was collected and mixed with 100 μL of D_2O and 0.05 μL of dimethyl sulfoxide (DMSO). No liquid products were detected. Electrochemical surface areas (ECSAs) were determined from double-layer capacitance (C_{dl}) measured by cyclic voltammetry. Electrochemical impedance spectroscopy (EIS) was carried out at an AC voltage amplitude of 5 mV over a frequency range of 0.01 to 100 kHz.

$^{13}CO_2$ isotopic labeling experiment

To verify that the CO product originates from CO_2 electroreduction rather than from catalyst degradation or oxidation, a $^{13}CO_2$ isotopic labeling experiment was performed. $^{12}CO_2$ was replaced with $^{13}CO_2$, and potentiostatic electrolysis was conducted at –0.8 V in the H-type cell using PCNF for one hours. The effluent gas was analyzed by gas chromatography-mass spectrometer (GC-MS, Agilent 7890B-5977B).

Electrochemical measurements in a flow cell

ECR measurements at high current densities were conducted in a flow cell. To prepare the working electrode, 3 mg of catalyst and 20 μL of Fumion solution were dispersed in 480 μL of N,N-dimethylformamide under ultrasonication for 0.5 h. The resulting catalyst ink (160 μL) was drop-coated onto a gas diffusion layer (YLS30T, 1 cm^2) to achieve a catalyst loading of 0.96 mg cm^{-2}. A Ag/AgCl electrode and a platinum sheet served as the reference and counter electrodes, respectively, in a three-electrode flow cell configuration. Both the anolyte and catholyte were 1 M KOH, separated by an anion exchange membrane (FAB-PK-130). During the electrochemical testing, the CO_2 gas flow rate was maintained at 25 mL min^{-1}, while the electrolyte at both the anode and cathode was continuously circulated at 20 mL min^{-1}. To compensate for potential drops

arising from solution resistance (R_s), ohmic drop correction was applied. All reported potentials were converted to the RHE scale using the following equation:

$$E\ (iR\text{-corrected vs. RHE}) = E\ (\text{vs. RHE}) - iR_s \quad (2)$$

Faradaic efficiency calculation

The faradaic efficiencies (FEs) for CO and H_2 products were using the following equation:

$$\text{FE} = (n \times V \times v \times F \times P) / (I \times R \times T) \quad (3)$$

where n is number of electrons transferred to form one product molecule; V is the volume proportion of the product determined by GC; v is the gas flow rate (10 mL min^{-1}); F is the Faraday constant (96485 C mol^{-1}); P is the atmospheric pressure (1.013×10^5 Pa); I is the measured current; R is the gas constant (8.314 J mol^{-1} K^{-1}); T is the room temperature (298.15 K).

Computational methods

Density functional theory (DFT) calculations were performed using Vienna Ab-initio Simulation Package (VASP 6.1.0).[1–4] Geometry optimization and electronic properties were calculated using projector augmented wave (PAW) pseudo-potentials. The generalized gradient approximation (GGA) in the Perdew-Burke-Ernzerh (PBE) formulation was used for the exchange-correlation functional. The electron wave functions were expanded with a kinetic energy cutoff of 450 eV. Based on the physicochemical characterization, F primarily bonds with C to form C–F bonds. Accordingly, C–F bonds were constructed on vertically oriented graphene planes in different N-doped models to investigate the effect of F on electronic structure modulation. A vacuum layer of 20 Å along the z-axis was introduced to avoid interactions between periodic images. The Brillouin zone was sampled using a Monkhorst-Pack grid of 3 × 3 × 1 centred at the Gamma point. Self-

consistent field iterations were converged to a total energy change of less than 10^{-4} eV, and the force convergence threshold was set to 0.02 eV $Å^{-1}$ per atom.

The adsorption energy (AE) of each adsorbate was calculated using the following equation:

$$AE = E(\text{slab–adsorbate}) - E(\text{slab}) - E(\text{adsorbate}) \quad (4)$$

where E(adsorbate), E(slab), and E(slab–adsorbate) are the energies of the free adsorbate in the gas phase, the clean slab, and the adsorbed system, respectively.

Gibbs free energies were calculated using the following equation:

$$G = E + ZPE - TS \quad (5)$$

where T is 298.15 K; E is the DFT-based total energy, and ZPE and S are the zero-point energy and entropy of the species, respectively.[5]

The two–electron catalytic mechanism for ECR to CO is as follows:

$$CO_2 + 2(H^+ + e^-) + * \rightarrow *COOH + (H^+ + e^-) \quad (6)$$

$$*COOH + (H^+ + e^-) \rightarrow *CO + H_2O \quad (7)$$

$$*CO \rightarrow CO + * \quad (8)$$

where * denotes the active site.

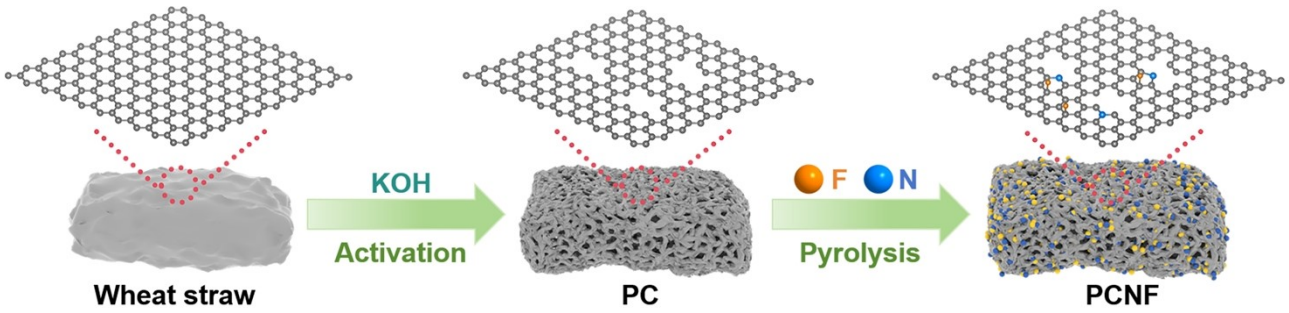

Fig. S1 Schematic diagram of the preparation process of PCNF.

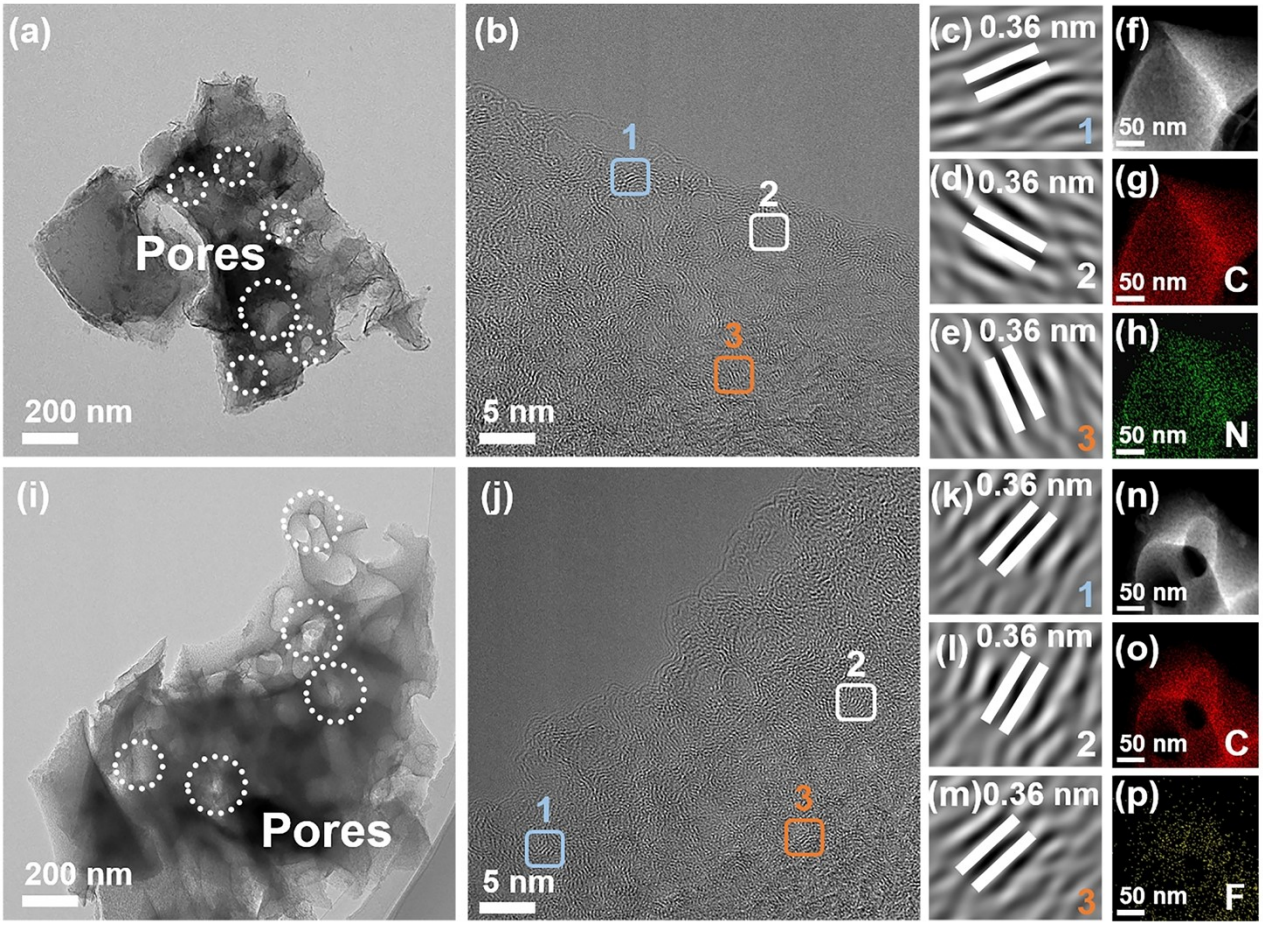

Fig. S2 (a,b) TEM images of PCN. (c–e) Lattice fringes from the three regions highlighted in (b). (f–h) Elemental mapping images of PCN. (i,j) TEM images of PCF. (k–m) Lattice fringes from the three regions highlighted in (j). (n–p) Elemental mapping images of PCF.

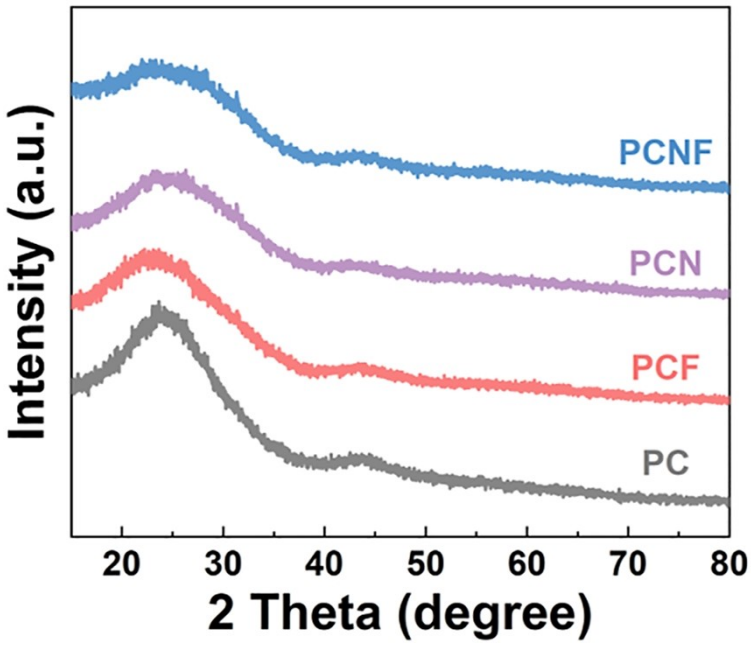

Fig. S3 XRD patterns of PCNF, PCN, PCF, and PC.

Note: XRD patterns (Fig. S3) show diffraction peaks at approximately 24° and 43° for all samples, which can be assigned to the (002) and (100) planes of graphitic carbon, respectively.[6] The lower (002) peak intensities for PCNF, PCN, and PCF relative to PC indicate insertion of N and/or F into the carbon lattice and a consequent decrease in graphitization.

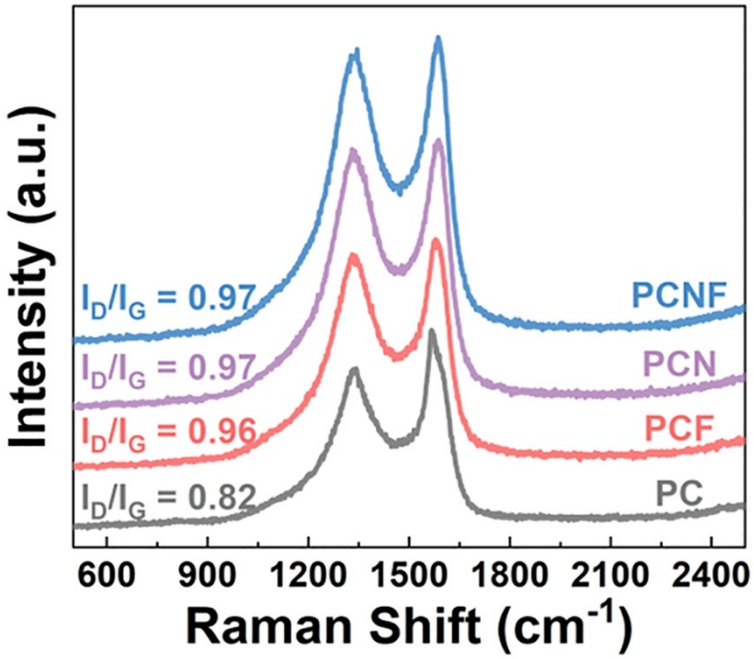

Fig. S4 Raman spectra of PCNF, PCN, PCF, and PC.

Note: Raman spectra (Fig. S4) reveal higher I_D/I_G ratios for these heteroatom-doped samples than for PC, consistent with increased defect density upon F and/or N doping.[7]

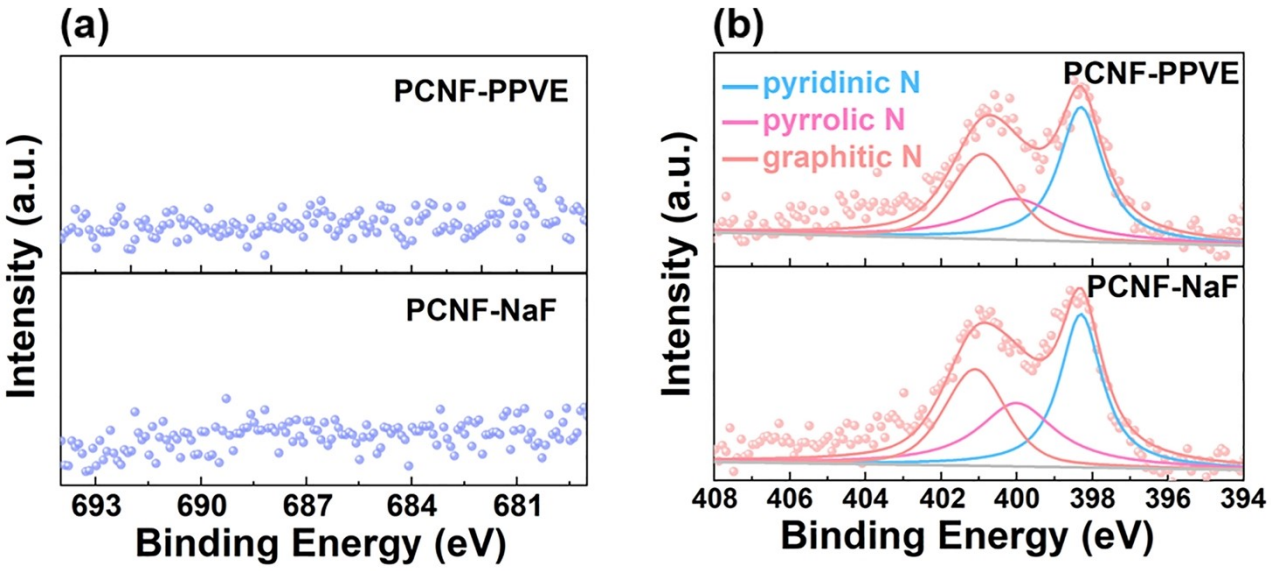

Fig. S5 High-resolution XPS (a) F 1s and (b) N 1s spectra of PCNF-PPVE and PCNF-NaF.

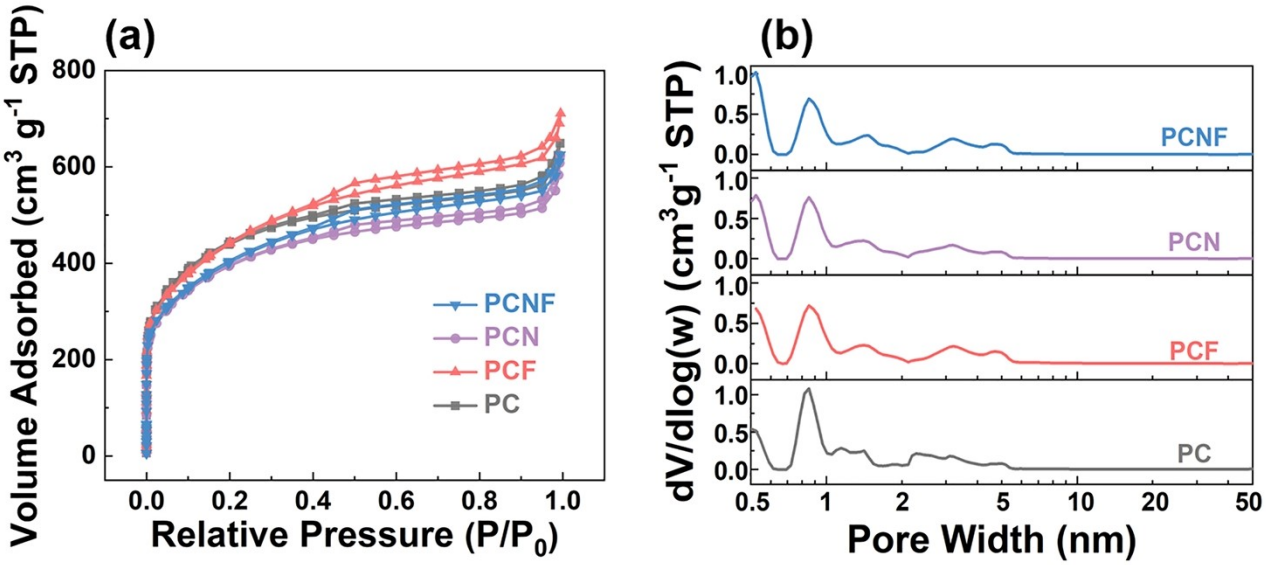

Fig. S6 (a) N_2 adsorption-desorption isotherms and (b) pore width distribution curves of PCNF, PCN, PCF, and PC.

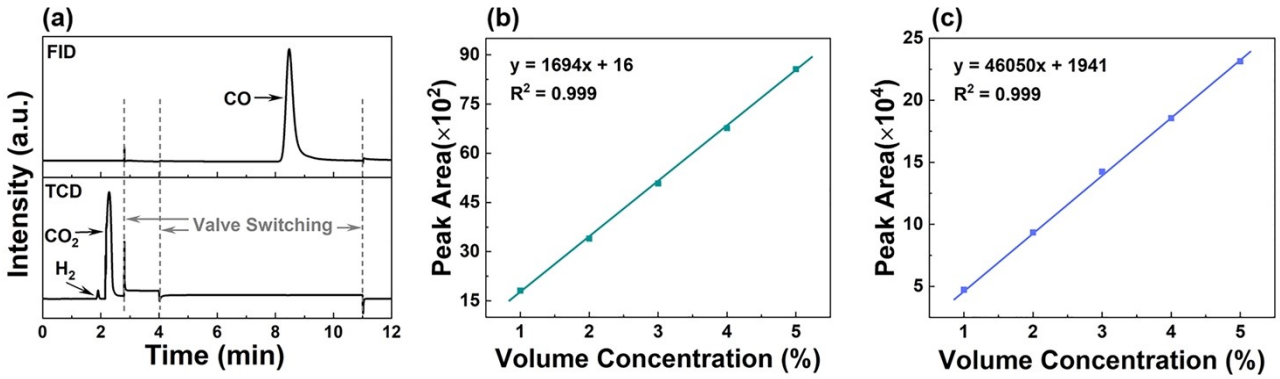

Fig. S7 (a) Representative GC chromatogram of gaseous products from PCNF at –0.8 V. Standard calibration curves for (b) H_2 and (c) CO.

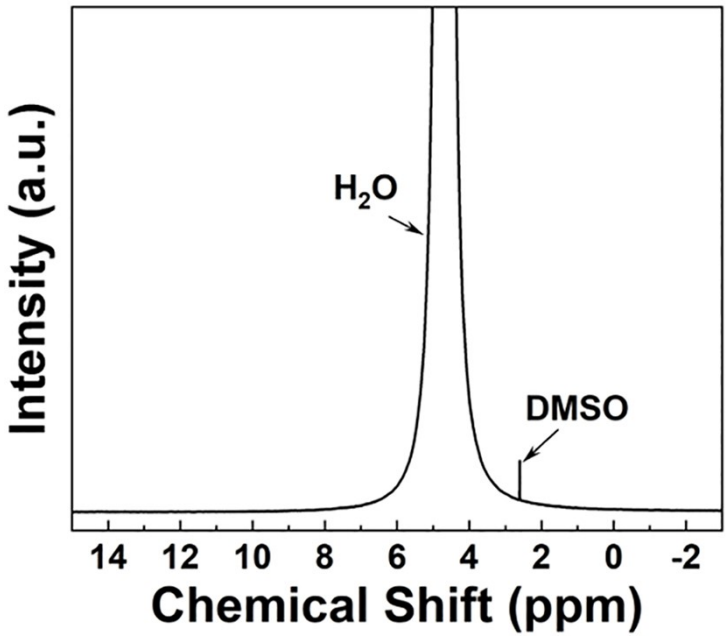

Fig. S8 Typical ^{1}H NMR spectrum of the electrolyte after electrolysis of PCNF at –0.8 V.

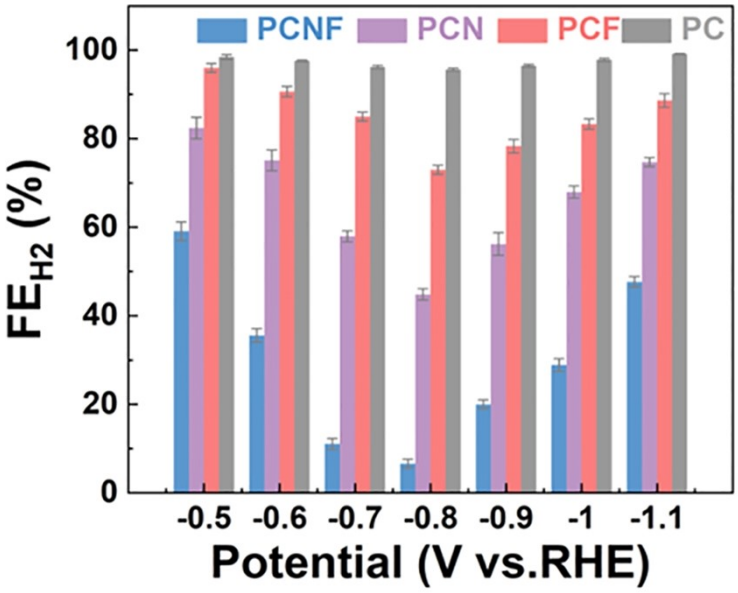

Fig. S9 FE_{H2} of PCNF, PCN, PCF, and PC at different potentials.

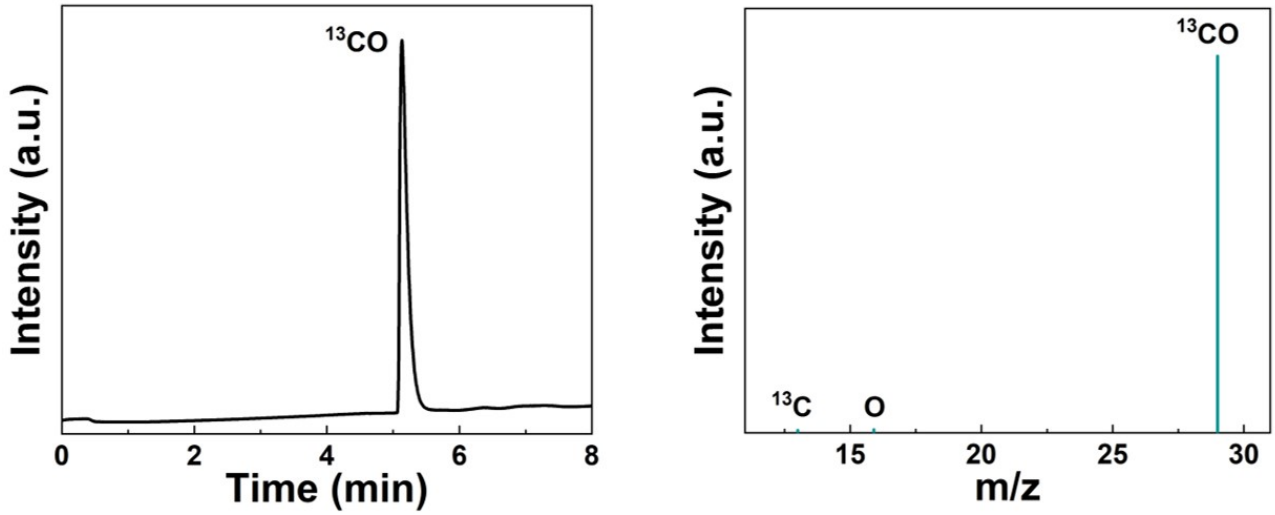

Fig. S10 GC-MS analysis of the gaseous products from PCNF after electrolysis under a $^{13}CO_2$ atmosphere at –0.8 V.

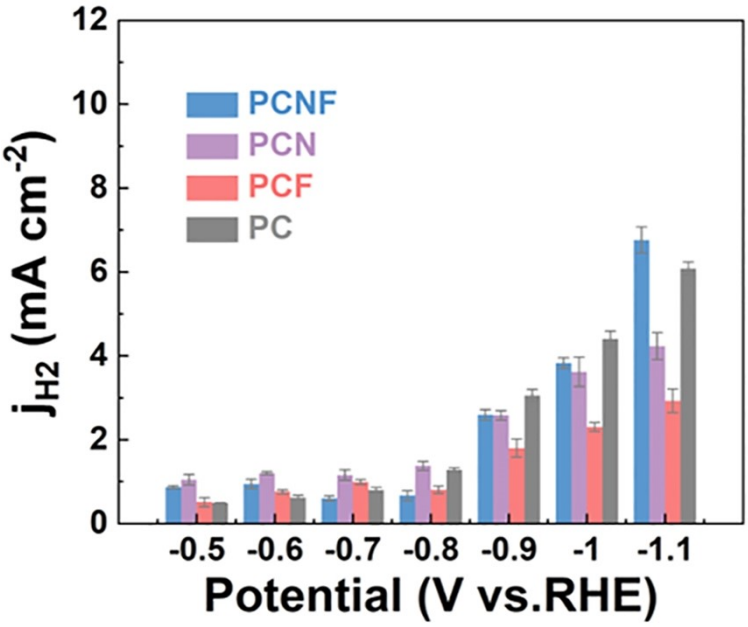

Fig. S11 j_{H2} of PCNF, PCN, PCF, and PC at different potentials.

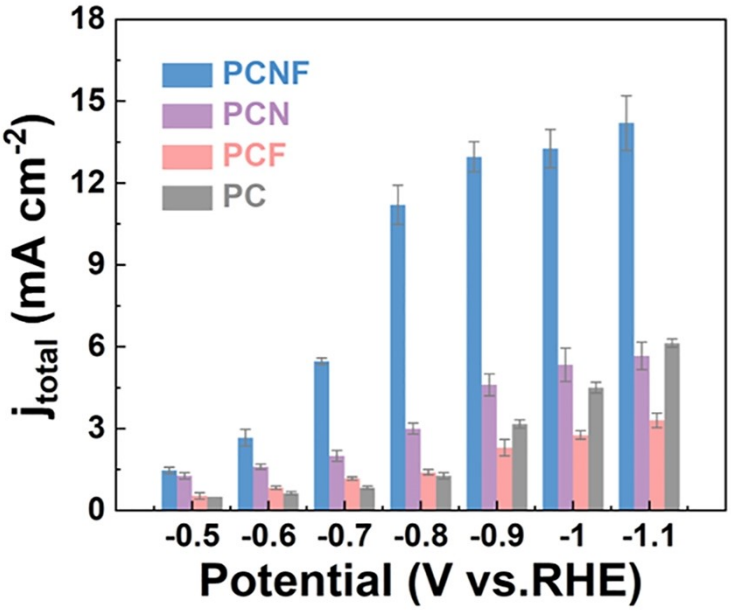

Fig. S12 Total current density (j_{total}) of PCNF, PCN, PCF, and PC at various applied potentials.

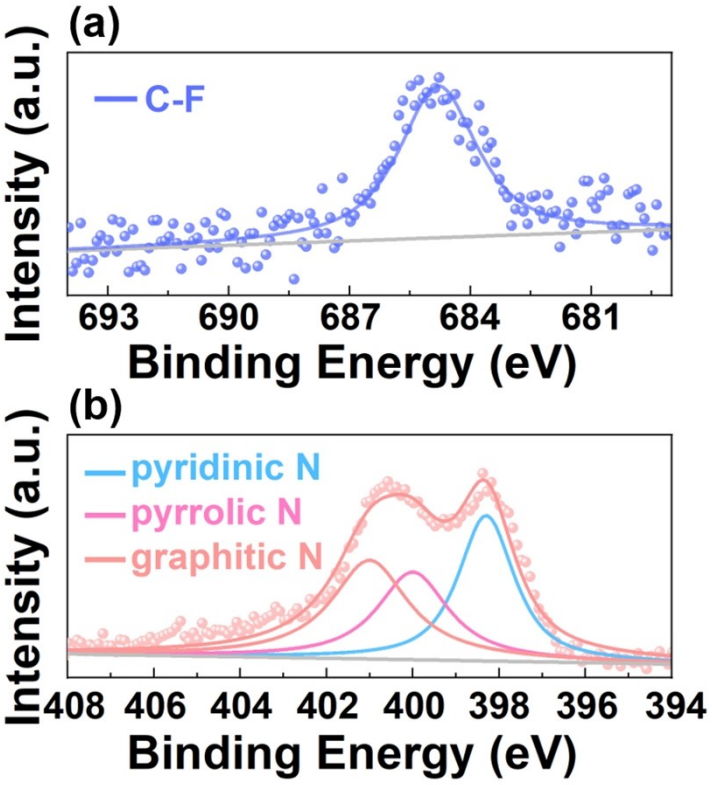

Fig. S13 High-resolution XPS (a) F 1s and (b) N 1s spectra of PCNF-plasma.

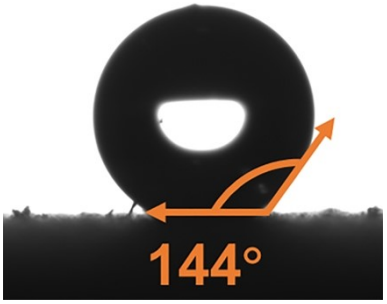

Fig. S14 Water contact angle image of PCNF-plasma (144°).

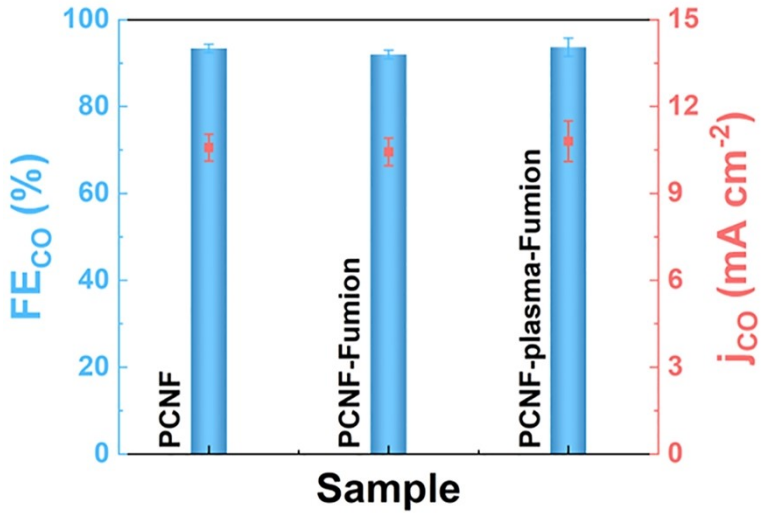

Fig. S15 FE_{CO} and j_{CO} of PCNF, PCNF-Fumion, and PCNF-plasma-Fumion at –0.8 V.

Note: To verify that the hydrophobicity of PCNF stems from F incorporated into the carbon framework rather than from residual fluorinated surface species, we subjected PCNF to plasma treatment to remove its surface components. The resulting sample is designated PCNF-plasma. As shown in Fig. S13 and Fig. S14, PCNF-plasma and PCNF possess identical chemical states of N and F species and comparable water contact angles, confirming that the hydrophobicity of PCNF derives from F doped into the carbon framework rather than from residual fluorinated surface species. In addition, to exclude any contribution from the Nafion binder used in the electrochemical tests described above, working electrodes were fabricated using PCNF and PCNF-plasma as catalysts and an F-free Fumion solution (FAA-3-SOLUT-10) as the binder. These electrodes are designated PCNF-Fumion and PCNF-plasma-Fumion, respectively. As shown in Fig. S15, the FE_{CO} and j_{CO} of PCNF-Fumion and PCNF-plasma-Fumion are comparable to those of PCNF. Thus, the superior ECR performance of PCNF is attributed to the N and F atoms doped within the carbon framework and is independent of the binder type.

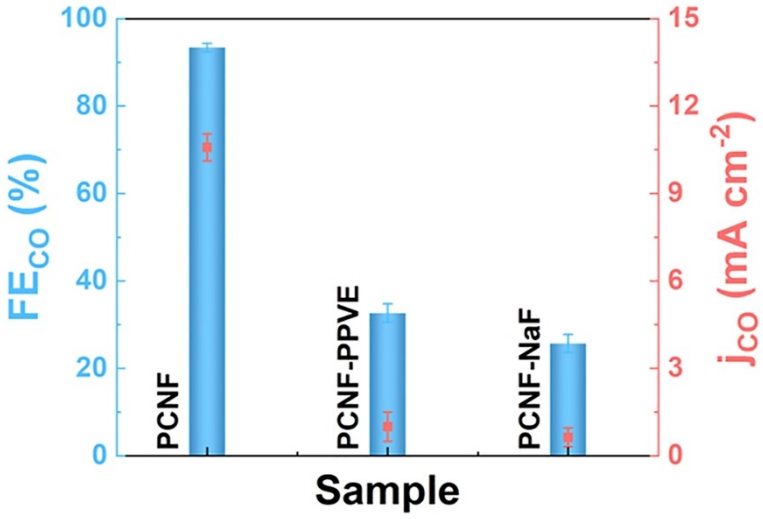

Fig. S16 FE_{CO} and j_{CO} of PCNF, PCNF-PPVE, and PCNF-NaF at –0.8 V.

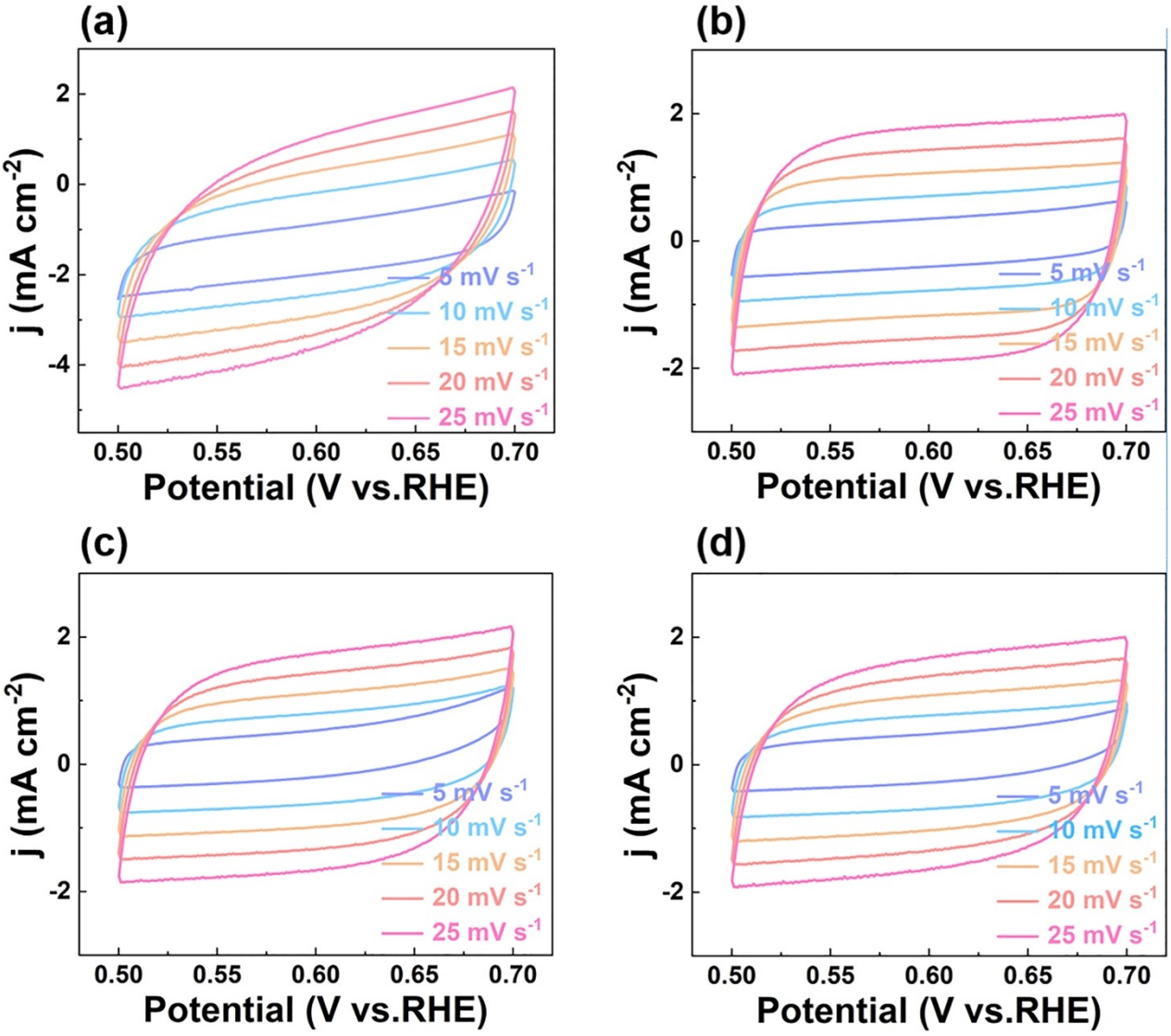

Fig. S17 Cyclic voltammetry curves at different scan rates of (a) PCNF, (b) PCN, (c) PCF, and (d) PC.

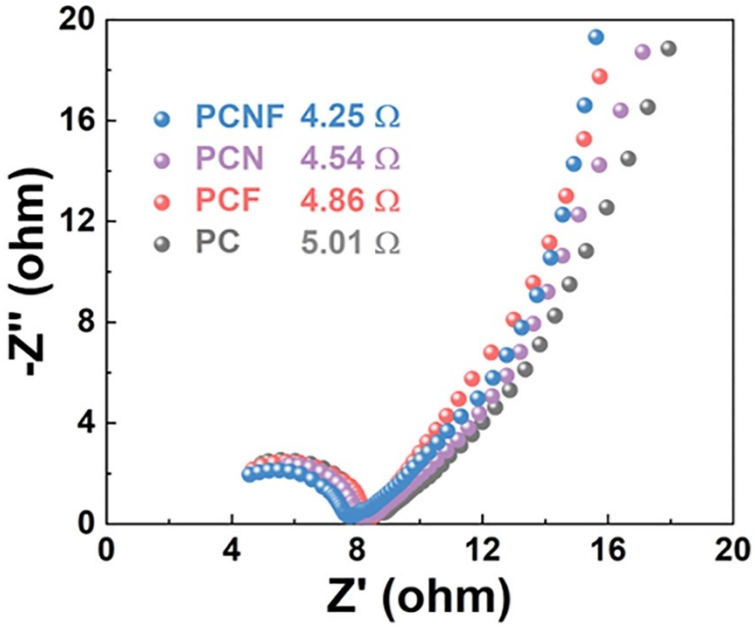

Fig. S18 Nyquist plots of PCNF, PCN, PCF, and PC.

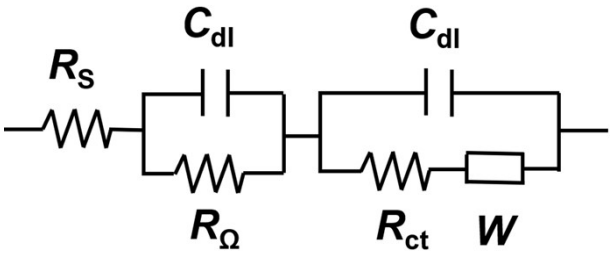

Fig. S19 Equivalent circuit model (R_s: solution resistance, C_{dl}: double-layer capacitance, R_Ω: ohmic resistance, R_{CT}: charge transfer resistance, W: Warburg impedance).

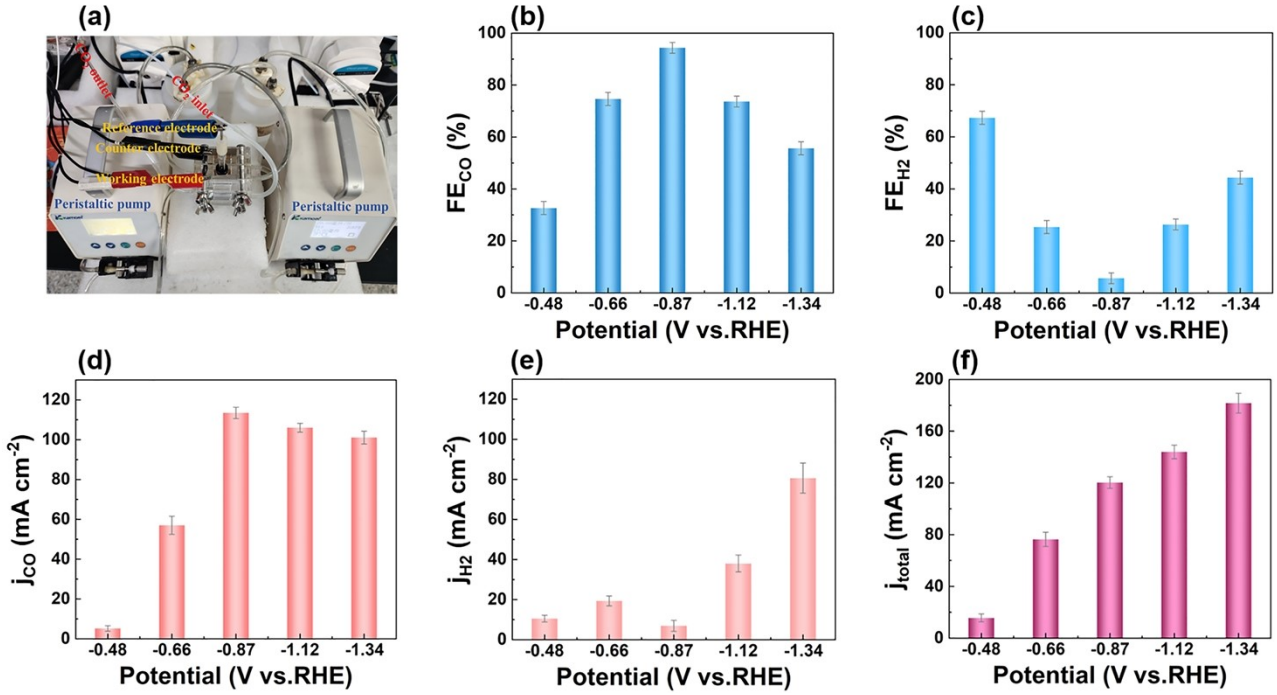

Fig. S20 (a) Photograph of the flow cell. (b) FE_{CO}, (c) FE_{H2}, (d) j_{CO}, (e) j_{H2}, and (f) j_{total} of PCNF at various applied potentials in the flow cell.

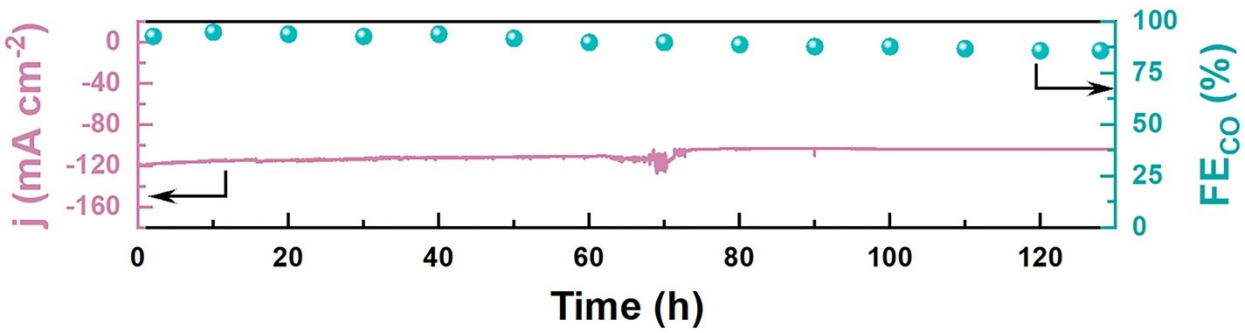

Fig. S21 Electrochemical stability of PCNF measured at –0.87 V in the flow cell over 130 hours.

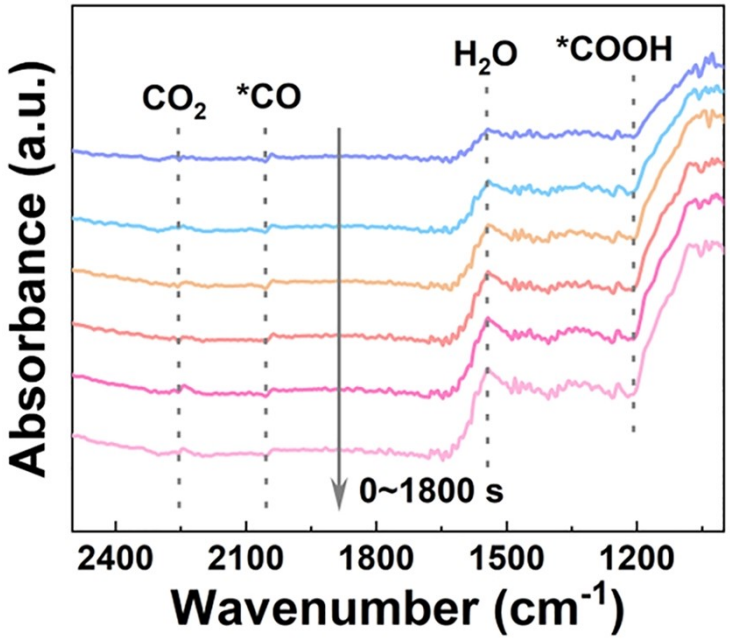

Fig. S22 *In situ* ATR-SEIRAS spectra of PC measured at –0.8 V.

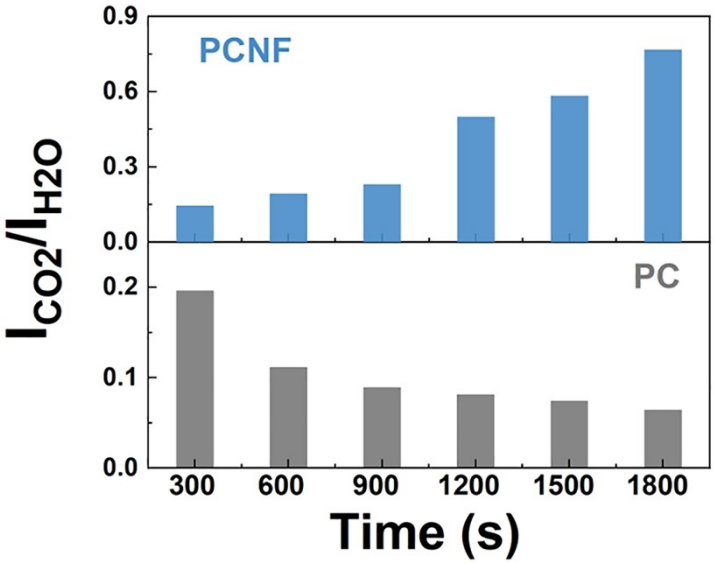

Fig. S23 Peak intensity ratios of CO_2 to H_2O (I_{CO2}/I_{H2O}) for PCNF and PC as a function of electrolysis time.

Note: the CO_2 peak of PCNF (near 2270 cm^{-1}) intensifies progressively with electrolysis time (Fig. 3f),[8] signalling sustained CO_2 enrichment at the catalyst surface. Meanwhile, the peak intensity ratio of CO_2 to H_2O (I_{CO2}/I_{H2O}) for PCNF rises steadily (Fig. S23). This trend indicates that during electrolysis, CO_2 diffuses readily from the bulk solution to the PCNF surface, whereas the access of H_2O/H^+ is impeded, resulting in a locally elevated CO_2 concentration and a depleted H_2O/H^+ concentration. In stark contrast, PC exhibits a weaker CO_2 signal (Fig. S22), and a declining I_{CO2}/I_{H2O} ratio (Fig. S23), confirming that its relatively hydrophilic surface preferentially accumulates H_2O/H^+ over CO_2. These direct spectroscopic observations validate the dual role of F-induced hydrophobicity: it enriches CO_2 while excluding H_2O/H^+ from the catalyst interface.

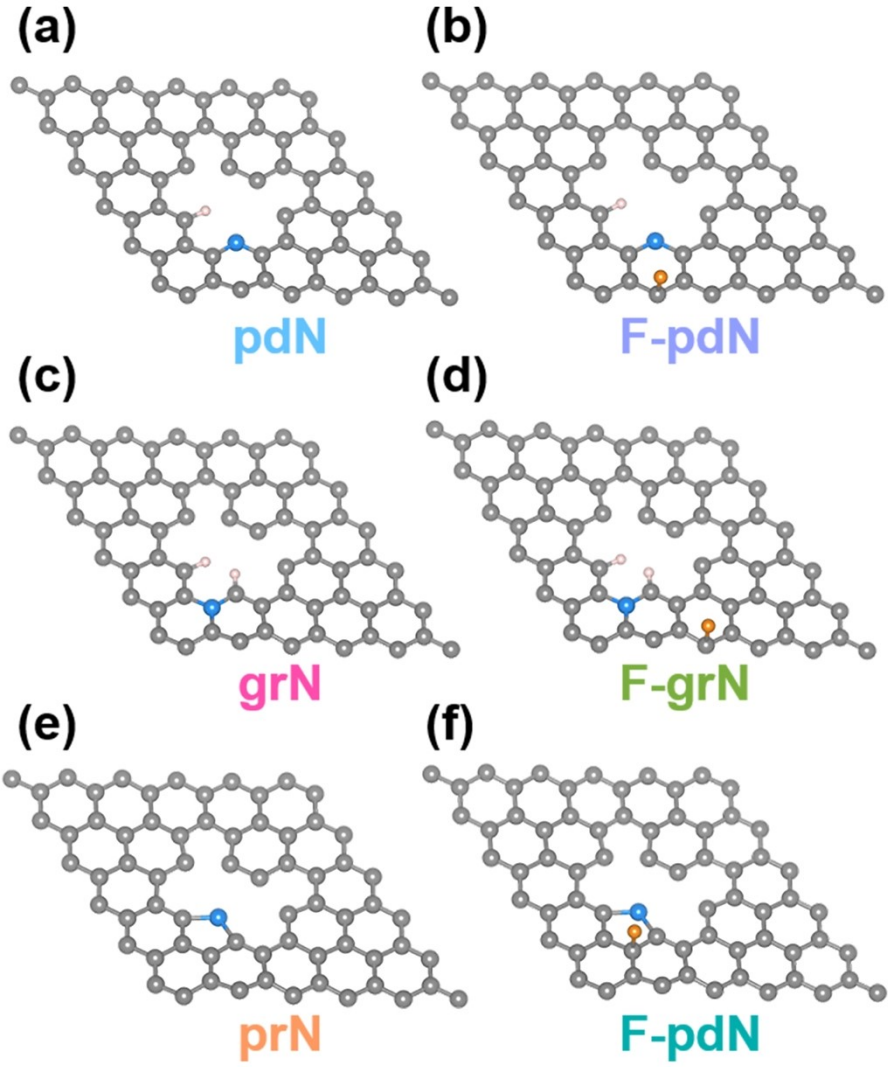

Fig. S24 Optimized structures of pyridinic, graphitic, and pyrrolic N and their fluorinated counterparts. (a) pdN, (b) F-pdN, (c) grN, (d) F-grN, (e) prN, (f) F-prN. (grey: C, blue: N, yellow: F, white: H)

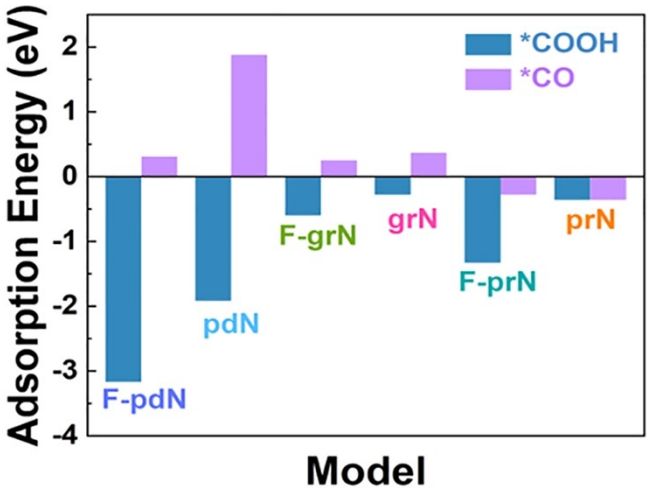

Fig. S25 Calculated adsorption energies of *COOH and *CO on the model surfaces.

Table S1. Atomic contents of N and F in PCNF, PCN, and PCF determined by XPS.

Sample	N (at%)	F (at%)
PCNF	2.62	0.42
PCN	2.37	—
PCF	—	0.37
PCNF-PPVE	2.12	0.13
PCNF-NaF	1.85	0.11
PCNF-plasma	2.67	0.54

Table S2. Textural parameters of PCNF, PCN, PCF, and PC.

Sample	S_{BET} ($m^2\ g^{-1}$)	V_{total} ($cm^3\ g^{-1}$)	$S_{micropore}$ ($m^2\ g^{-1}$)	$V_{micropore}$ ($cm^3\ g^{-1}$)
PCNF	1445.9	0.97	871.1	0.40
PCN	1425.3	0.97	934.0	0.42
PCF	1588.3	0.99	791.6	0.35
PC	1594.6	0.99	1108.2	0.49

Note: As summarized in Table S2, PCNF, PCN, PCF, and PC possess comparable specific surface areas and pore volumes, but their ECR performance differs markedly (Fig. 3b and Fig. 3c). This indicates that the performance differences originate primarily form the intrinsic activity of the active sites and the nature of the microenvironment, rather than from textural properties. Raman spectra (Fig. S4) show that PCNF, PCN, and PCF have similar I_D/I_G ratios, suggesting comparable defect densities among the three doped samples. Nevertheless, PCNF substantially outperforms PCN and PCF in both FE_{CO} and j_{CO}. Furthermore, although PC contains no N or F heteroatoms, it possesses the largest specific surface area and pore volume, and its I_D/I_G value of 0.87 indicates a considerable number of surface defects. Despite these features, PC exhibits negligible ECR activity. Defect density is therefore not the primary origin of the excellent ECR activity and selectivity of PCNF. Instead, the electronic and hydrophobic effects of F are the key factors.

Table S3. Comparison of ECR performance of PCNF with previously reported catalysts.

Catalyst	Electrolyte	[a]Potential (V vs. RHE)	[b]FE_{CO} (%)	[c]j_{CO} (mA cm^{-2})	Ref.
NFCNT	0.1 M $KHCO_3$	–0.55	94	3.6	9
NF-C	0.1 M $KHCO_3$	–0.60	90	1.9	10
N,F-CB	0.1 M $KHCO_3$	–0.70	93	4.6	11
ANC-1-1	0.1 M $KHCO_3$	–0.61	90.5	5.6	12
NPC-900	0.5 M $KHCO_3$	–0.67	95	2.3	13
CNPC-1100	0.1 M $KHCO_3$	–0.60	92	0.3	14
NS-C-900	0.1 M $KHCO_3$	–0.60	92	2.6	15
NSHPC	0.1 M $KHCO_3$	–0.62	87.9	2.8	16
Ni-SAC	0.1 M $KHCO_3$	–0.80	98	1	17
FC	0.1 M $KHCO_3$	–0.62	89.6	0.3	18
WNCNs-100	0.1 M $KHCO_3$	–0.60	84	1.2	19
NC-27	0.1 M $KHCO_3$	–0.71	75	1.5	20
2D-pg-C_3N_4	2 M $KHCO_3$	–0.35	80	2.5	21
N-hCNC	0.5 M $KHCO_3$	–0.6	83.6	2	22
NBMC-1000	0.1 M $KHCO_3$	–0.55	95	2.7	23
NSCNW-3	0.1 M $KHCO_3$	–0.60	93.4	5.9	24
Co-N_5/HNPCSs	0.2 M $NaHCO_3$	–0.79	99	6.2	25
PCNF	0.5 M $KHCO_3$ (H-type cell)	–0.8	93	10.5	This work
	1M KOH (flow cell)	–0.87	94	113	

[a] Potential at which the maximum FE_{CO} is achieved. [b] Maximum FE_{CO}. [c] j_{CO} at the potential in [a].

References

1 G. Kresse and J. Hafner, *Phys. Rev. B*, 1993, **47**, 558–561.

2 G. Kresse and J. Hafner, *Phys. Rev. B*, 1994, **49**, 14251–14269.

3 G. Kresse and J. Furthmuller, *Comput. Mater. Sci.*, 1996, **6**, 15–50.

4 G. Kresse and J. Furthmuller, *Phys. Rev. B*, 1996, **54**, 11169–11186.

5 V. Wang, N. Xu, J. –C. Liu, G. Tang and W. –T. Geng, *Comput. Phys. Commun.*, 2021, **267**, 108033.

6 P. Bai and L. Xu, *Appl. Catal. B*, 2025, **365**, 124908.

7 W. Liu, P. Bai, S. Wei, C. Yang and L. Xu, *Angew. Chem. Int. Ed.*, 2022, **61**, e202201166.

8 Y. Lin, C. Xia, Z. Zhu, J. Wang, H. Niu, S. Gong, Z. Li, N. Yang, J. Song Chen, R. Wu and B. Y. Xia, *Angew. Chem. Int. Ed.*, 2025, **64**, e202414569.

9 J. Han, L. Shi, H. Xie, R. Song, D. Wang and D. Liu, *Small*, 2024, **20**, 2401766.

10 F. Pan, B. Li, X. Xiang, G. Wang and Y. Li, *ACS Catal.*, 2019, **9**, 2124–2133.

11 H. Chen, Y. Zhang, T. Yang, Y. Shang, Q. Zhu, S. Cao, X. Lin, S. Liu, S. Wei, B. Wei, Z. Wang and X. Lu, *Dalton. Trans.*, 2022, **51**, 15883–15888.

12 Z. Zhou, P. Xia, Y. Tan, S. Xiao, Y. Xue, J. Li and G. Yang, *Catal. Lett.*, 2024, **154**, 4044–4054.

13 W. Liu, J. Qi, P. Bai, W. Zhang and L. Xu, *Appl. Catal. B*, 2020, **272**, 118974.

14 C. Li, Y. Wang, N. Xiao, H. Li, Y. Ji, Z. Guo, C. Liu and J. Qiu, *Carbon*, 2019, **151**, 46–52.

15 F. Pan, B. Li, W. Deng, Z. Du, Y. Gang, G. Wang and Y. Li, *Appl. Catal. B*, 2019, **252**, 240–249.

16 R. Li, F. Liu, Y. Zhang, M. Guo and D. Liu, *ACS Appl. Mater. Interfaces*, 2020, **12**, 44578–44587.

17 H. Yang, L. Shang, Q. Zhang, R. Shi, G. I. N. Waterhouse, L. Gu and T. Zhang, *Nat. Commun.*, 2019, **10**, 4585.

18 J. Xie, X. Zhao, M. Wu, Q. Li, Y. Wang and J. Yao, *Angew. Chem. Int. Ed.*, 2018, **57**, 9640–9644.

19 H. Li, N. Xiao, M. Hao, X. Song, Y. Wang, Y. Ji, C. Liu, C. Li, Z. Guo, F. Zhang and J. Qiu, *Chem. Eng. J.*, 2018, **351**, 613–621.

20 D. Hursan, A. A. Samu, L. Janovak, K. Artyushkova, T. Asset, P. Atanassov and C. Janaky, *Joule*, 2019, **3**, 1719–1733.

21 B. Zhang, T.–J. Zhao, W.–J. Feng, Y.–X. Liu, H.–H. Wang, H. Su, L.–B. Lv, X.–H. Li and J.–S. Chen, *Nano Res.*, 2018, **11**, 2450–2459.

22 L. Jiao, C. Mao, B. Feng, F. Xu, S. Li, J. Zhong, M. Xia, R. Cui, X. Wang, L. Yang, Q. Wu and Z. Hu, *Nano Res.*, 2025, **18**, 94907171.

23 X. Ma, J. Du, H. Sun, F. Ye, X. Wang, P. Xu, C. Hu, L. Zhang and D. Liu, *Appl. Catal. B*, 2021, **298**, 120543.

24 H. Han, S. Park, D. Jang, S. Lee and W. B. Kim, *ChemSusChem*, 2020, **13**, 539–547.

25 Y. Pan, R. Lin, Y. Chen, S. Liu, W. Zhu, X. Cao, W. Chen, K. Wu, W. C. Cheong, Y. Wang, L. Zheng, J. Luo, Y. Lin, Y. Liu, C. Liu, J. Li, Q. Lu, X. Chen, D. Wang, Q. Peng, C. Chen and Y. Li, *J. Am. Chem. Soc.*, 2018, **140**, 4218–4221.